Journal of Microscopy

Journal of Microscopy, Vol. 00, Issue 00 2019, pp. 1–10
Received 16 September 2019; accepted 27 November 2019

doi: 10.1111/jmi.12850

Nanocrystal segmentation in scanning precession electron diffraction data

T. BERGH*, D.N. JOHNSTONE†, P. CROUT†, S. HØGÅS*, P.A. MIDGLEY†, R. HOLMESTAD*, P.E. VULLUM*,‡ & A.T.J. VAN HELVOORT*

**Department of Physics, Norwegian University of Science and Technology (NTNU), Trondheim, Norway*
†Department of Materials Science and Metallurgy, University of Cambridge, Cambridge, U.K.
‡Department of Materials and Nanotechnology, SINTEF Industry, Trondheim, Norway

Key words. Nanoparticles, non-negative matrix factorization, open-source, scanning precession electron diffraction, virtual dark-field imaging, watershed segmentation.

Summary

Scanning precession electron diffraction (SPED) enables the local crystallography of materials to be probed on the nanoscale by recording a two-dimensional precession electron diffraction (PED) pattern at every probe position as a dynamically rocking electron beam is scanned across the specimen. SPED data from nanocrystalline materials commonly contain some PED patterns in which diffraction is measured from multiple crystals. To analyse such data, it is important to perform *nanocrystal segmentation* to isolate both the location of each crystal and a corresponding representative diffraction signal. This also reduces data dimensionality significantly. Here, two approaches to nanocrystal segmentation are presented, the first based on virtual dark-field imaging and the second on non-negative matrix factorization. Relative merits and limitations are compared in application to SPED data obtained from partly overlapping nanoparticles, and particular challenges are highlighted associated with crystals exciting the same diffraction conditions. It is demonstrated that both strategies can be used for nanocrystal segmentation without prior knowledge of the crystal structures present, but also that segmentation artefacts can arise and must be considered carefully. The analysis workflows associated with this work are provided open-source.

Introduction

Scanning electron diffraction (SED) is a scanning transmission electron microscopy technique in which a two-dimensional electron diffraction pattern is acquired at each probe position as a nanometre sized electron probe is scanned across a region of interest. Double-conical rocking of the electron probe may also be incorporated to record a precession electron diffraction (PED) pattern (Vincent & Midgley, 1994) at each probe position [scanning precession electron diffraction (SPED)] (Rauch *et al.*, 2010). Analysis of SED and SPED data is typically similar, enabling the assessment of local crystallography on the nanoscale by, for instance, crystal phase (Mu *et al.*, 2016), orientation (Zaefferer, 2011) and strain mapping (Rouviere *et al.*, 2013; Cooper *et al.*, 2016). S(P)ED data obtained from nanocrystalline materials typically comprise a relatively large number of (P)ED patterns, ca. 100–500 000, recorded from a significantly smaller number of crystals, ca. 10–1000. Such data frequently include some (P)ED patterns that contain scattering from multiple crystals sampled along the beam trajectory. To isolate the diffraction signals from individual crystals that may overlap in projection, *nanocrystal segmentation* can be performed.

Nanocrystal segmentation of S(P)ED data aims to isolate the real space location of each individual crystal in the scan region, as well as a corresponding representative diffraction pattern for each crystal. This is a necessary step in analyzing the diffraction from each crystal in a polycrystalline sample and leads to substantial dimensionality reduction. Such segmentation therefore provides a route to overcome limitations associated with two-dimensional phase and orientation mapping in samples where crystal overlap is prominent (Kobler & Kübel, 2017). Nanocrystal segmentation is also a crucial step in reconstructing the morphology and diffraction pattern of each crystal in a polycrystalline specimen in three dimensions by scanning electron diffraction tomography (Eggeman *et al.*, 2015; Meng & Zuo, 2016).

Strategies for nanocrystal segmentation based on iterative indexation (Valery *et al.*, 2017), data matrix factorization (Eggeman *et al.*, 2015; Martineau *et al.*, 2019), virtual

Correspondence to: A.T.J. van Helvoort, Department of Physics, Norwegian University of Science and Technology (NTNU), Høgskoleringen 5, 7491 Trondheim, Norway. Tel.: +47 904 03 716; e-mail: a.helvoort@ntnu.no

dark-field (VDF) imaging (Meng & Zuo, 2016) and data clustering (Einsle *et al.*, 2018; Gallagher-Jones *et al.*, 2019; Martineau *et al.*, 2019) have been reported for S(P)ED data. Indexation requires knowledge of crystal structures present in the specimen, whereas clustering typically requires iterative determination of the number of categories. In contrast, VDF imaging and data matrix factorization approaches can be performed without such *a priori* knowledge, which makes them well suited to the study of unknown phases, and they are therefore the focus of this work. It has also been demonstrated that SPED data are typically more amenable to successful nanocrystal segmentation than SED data (Martineau *et al.*, 2019). This owes primarily to the integration through crystal bending and the reduction of dynamical oscillations in diffracted intensity as a function of thickness afforded by precession (Martineau *et al.*, 2019). Hence, the analysis of SPED data is central in the present work.

The VDF imaging approach (Meng & Zuo, 2016) is based on forming VDF images for numerous different diffraction conditions by plotting the integrated intensity of selected reflections as a function of probe position. The VDF images are compared against each other to identify images that show the same crystal, and such images are merged to yield one real space diffraction contrast image of each crystal. Simultaneously, the information on the associated diffraction conditions used to form each image in a merged set is combined to yield a representative diffraction pattern for that crystal.

The data matrix factorization approach is a form of unsupervised machine learning where all the (P)ED patterns are stacked as vectors in a data matrix, M, that is factorized into a factor matrix C_P and a loading matrix C_L. Non-negative matrix factorization (NMF) (Lee & Seung, 1999) is one such method that has been applied to S(P)ED data and found to yield factors that resemble (P)ED patterns, so-called component patterns, and loading maps that resemble diffraction contrast images highlighting the associated crystal in the scan region (Eggeman *et al.*, 2015; Martineau *et al.*, 2019).

In this work, VDF imaging and NMF are compared as methods for nanocrystal segmentation. Both approaches are applied to SPED data obtained from a model system composed of partly overlapping magnesium oxide (MgO) nanoparticles, where some crystals excite the same diffraction conditions. This system highlights particular challenges that arise when individual VDF images and individual loading maps are related to multiple crystals, which render the segmentation incomplete. To allow for a more complete nanocrystal segmentation, workflows incorporating image segmentation applied to VDF images or loading maps are developed. Relative merits and limitations of both strategies are discussed, and the associated SPED data (Bergh, 2019) and demonstrated workflows are available open-source (Johnstone *et al.*, 2019) for further application and development.

Methods

Specimen preparation

MgO was produced by burning a piece of Mg in air using a gas torch to obtain a smoke containing MgO nanoparticles. TEM grids coated by holey carbon were held in the smoke for ca. 2 s, so that MgO nanoparticles were deposited on the grids.

Scanning precession electron diffraction

SPED was performed using a JEOL JEM-2100F fitted with a Nanomegas ASTAR system. PED patterns were acquired using an externally mounted Stingray optical camera that imaged the phosphor viewing screen of the microscope. The microscope was operated at 200 kV with a convergence semi-angle of 1.0 mrad and a precession angle of 16 mrad. The precession frequency was 100 Hz and the exposure time at each probe position was 10 ms.

Data processing and analysis

SPED data were analysed using pyXem (Johnstone *et al.*, 2019), an open-source Python library for crystallographic electron microscopy, that builds on scientific Python packages, particularly hyperspy (de la Peña *et al.*, 2019), scikit-image (van der Walt *et al.*, 2014) and scikit-learn (Pedregosa *et al.*, 2011). A notebook including the workflows developed and parameters used (Johnstone *et al.*, 2019) and a copy of the associated SPED data (Bergh, 2019) have been made available open-source. The raw four-dimensional SPED dataset D_R had dimensions $(2X, 2Y|K_X, K_Y)$, where X and Y refer to the navigation dimensions, i.e. the dimensions of the scanned area, and K_X and K_Y refer to the signal dimensions, i.e. the dimensions of the PED patterns, following the notation used in hyperspy.

VDF imaging-based segmentation. The workflow for VDF imaging-based segmentation developed here was an adaption of the VDF imaging-based method proposed in Meng & Zuo (2016). The main difference was an additional step in which watershed image segmentation (Beucher & Lantuejoul, 1979) was applied to each of the VDF images, so that the method could be used in cases where individual VDF images showed multiple crystals. It should be noted that image segmentation could be achieved using a wide range of established strategies, and application of another strategy may further improve the approach. The complete data processing workflow is illustrated in Figure 1.

Preprocessing (Fig. 1A) included binning D_R in navigation space, which gave $D\,(X, Y|K_X, K_Y)$ that was aligned by shifting the centre of the direct beam to the same coordinates in all PED patterns. The background was removed by performing a

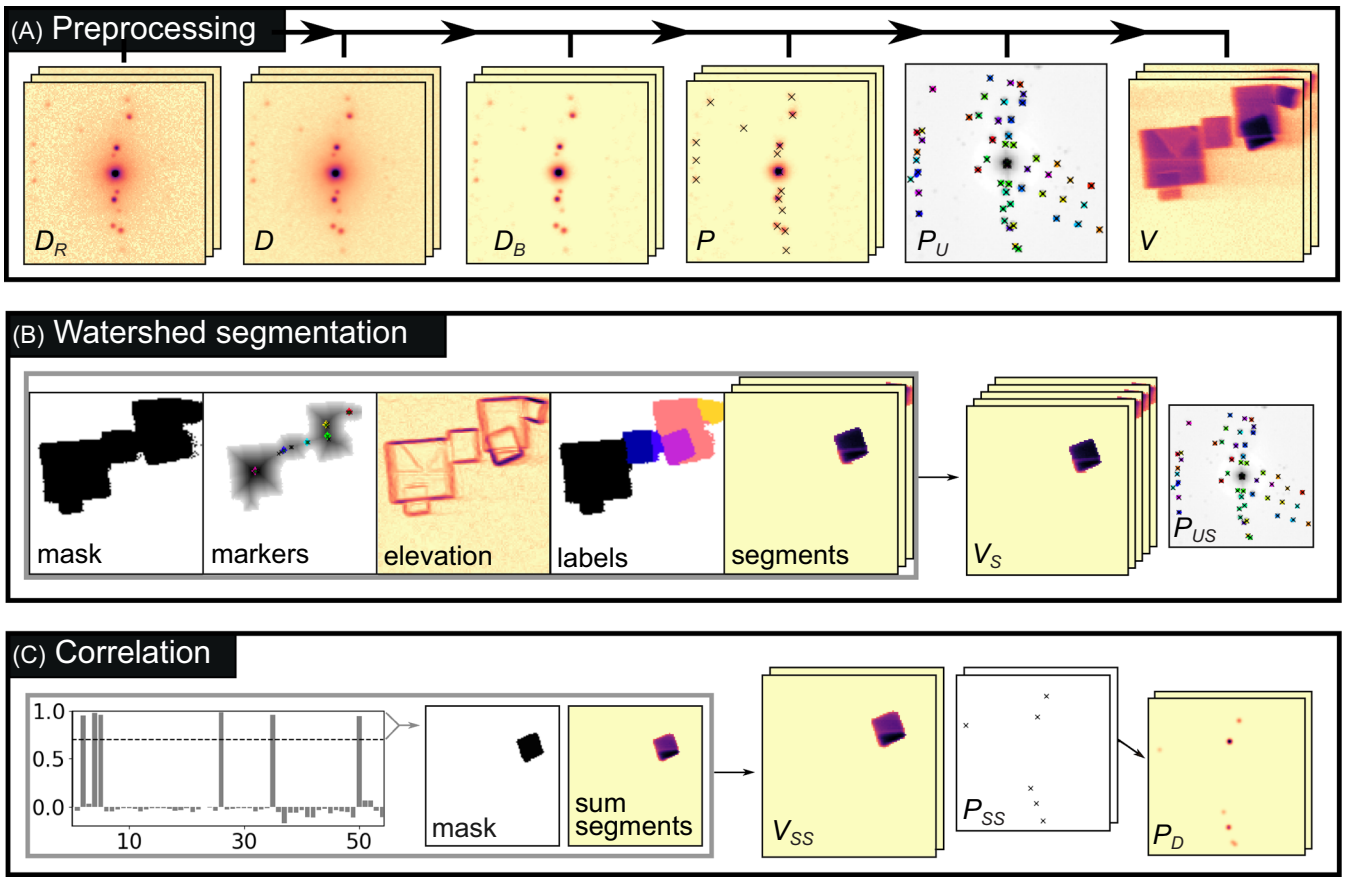

Fig. 1. Virtual dark-field (VDF) imaging-based segmentation workflow. (A) Preprocessing the raw data (D_R) by binning and alignment (D), before the background is removed (D_B), all peaks are found (P), unique peaks are determined (P_U) and VDF images (V) are formed for all unique peaks. (B) Watershed segmentation is performed on each VDF image to yield VDF image segments (V_S) with corresponding peaks (P_{US}). For each VDF image, a mask is formed, markers are determined and watershed segmentation is performed on the elevation image, leading to labelled regions that are used to define segments. (C) Correlation of the VDF image segments, where segments with a correlation exceeding a threshold are summed within a mask, leading to summed VDF image segments (V_{SS}) and corresponding peaks (P_{SS}). Virtual diffraction patterns (P_D) are created to visualize the diffraction spots of each summed segment.

difference of Gaussians background subtraction, which gave $D_B(X, Y|K_X, K_Y)$, before all diffraction peaks, $P(X, Y)$, were detected in all PED patterns, using a Laplacian of Gaussian blob finder. A clustering routine was employed to identify groups of peaks similar enough in positional coordinates to be considered to belong to the same unique diffraction vector. The unique vectors were filtered by magnitude to exclude the direct beam and diffraction peaks located at the edge of the detector, which resulted in N unique diffraction vectors, $P_U(N|2)$. VDF images were calculated by integrating the intensities within a disc centred at each of the unique peak positions in all PED patterns, which gave N VDF images $V(N|X, Y)$.

Each VDF image was segmented by the watershed method as depicted in Figure 1(B). For this, a mask was created by thresholding the VDF image automatically, the distance transform of the mask was calculated and its maxima were used in determination of markers for watershed. Further, an elevation image was calculated by applying the Sobel filter to the VDF image. The elevation image was segmented by watershed, which resulted in labelled regions. Labelled regions smaller than a user-defined *minimum size* were discarded, before a segment image was created for each labelled region based on the VDF image. Accordingly, applying the watershed segmentation routine to the VDF images yielded a stack of VDF image segments, $V_S(M|X, Y)$, and a corresponding list of unique vectors, $P_{US}(M|2)$, where $M \geq N$.

Cross-correlation was then performed between segments to identify those segments that corresponded to the same crystal, as illustrated in Figure 1(C). For the case demonstrated here, iterative comparisons of the correlation scores of one segment with the remaining segments were sufficient, although the full correlation matrix may be considered for improved accuracy in other cases. Segments with a normalized cross-correlation exceeding a user-specified *correlation threshold* were

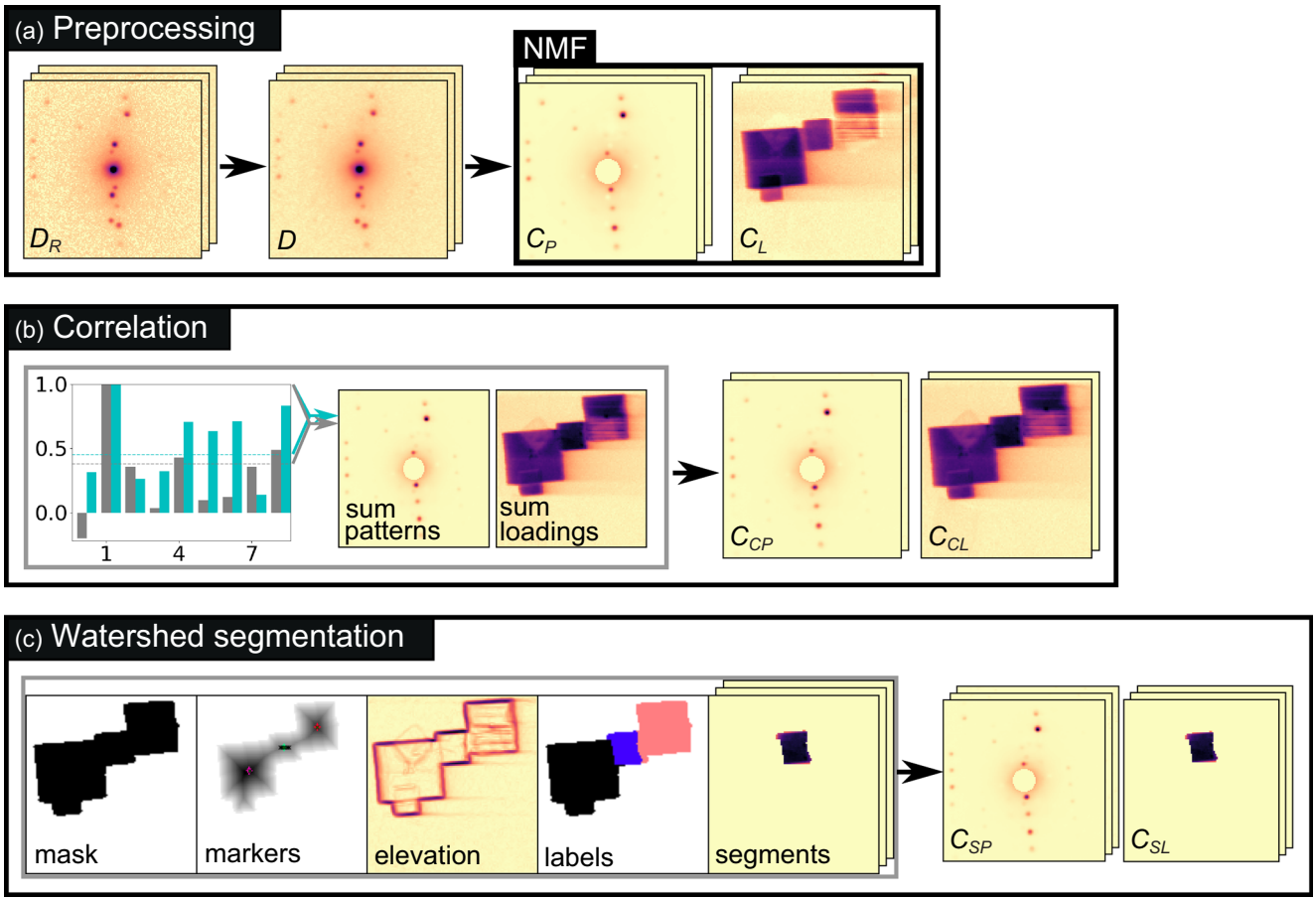

Fig. 2. Non-negative matrix factorization (NMF)-based segmentation workflow. (A) Preprocessing where the raw dataset (D_R) is binned and aligned (D). NMF performed on D yields component patterns (C_P) and loadings (C_L). (B) Correlation of the component patterns and loadings, where components are summed if the correlations of both patterns and factors exceed threshold values, leading to correlated patterns (C_{CP}) and loadings (C_{CL}). (C) Watershed segmentation is performed on each correlated loading to yield loading segments (C_{SL}) with corresponding patterns (C_{SP}). For each loading, a mask is formed, markers are determined and watershed segmentation is performed on the elevation image, leading to labelled regions that are used to define segments.

considered. If the number of these segments, which corresponded to the number of associated diffraction vectors, was below a user-specified *vector threshold*, the segments were discarded. Otherwise, a segment mask, defining the region where more segments than a user specified *segment threshold* had intensities above zero, was created, and the corresponding segments were summed within the segment mask. The segment sum was associated with its corresponding list of unique vectors, and each vector was assigned an intensity that was the total intensity of the corresponding single segment image within the segment mask. The correlation step resulted in a stack of summed segments, $V_{SS}(L|X, Y)$, and a list of diffraction vectors and intensities, $P_{SS}(L)$, where $L \leq M$. The final step was done for visualization purposes and consisted of reconstructing virtual diffraction patterns, $P_D(L|K_X, K_Y)$, for the summed segments, where Gaussians were used to model the diffraction spots.

NMF-based segmentation. The workflow for NMF-based segmentation is illustrated in Figure 2. The raw dataset, D_R, was binned and aligned to yield D, as for VDF imaging-based segmentation. D was decomposed by NMF following Poisson noise normalisation (Keenan & Kotula, 2004), as illustrated in Figure 2(A). The region in the centre of each PED pattern, including the direct beam, was masked prior to performing NMF. This masking improved NMF results by avoiding issues associated with the direct beam saturating the detector and by removing the influence of high intensity variations in the direct beam, which rank highly in the minimized error metrics computed during NMF without being related to the most crystallographically significant features in the data. To estimate the number of components, E, to use for NMF, a scree plot was inspected. The scree plot showed the fraction of total variance explained by each component obtained by singular value decomposition (SVD), after mean-centering of the PED

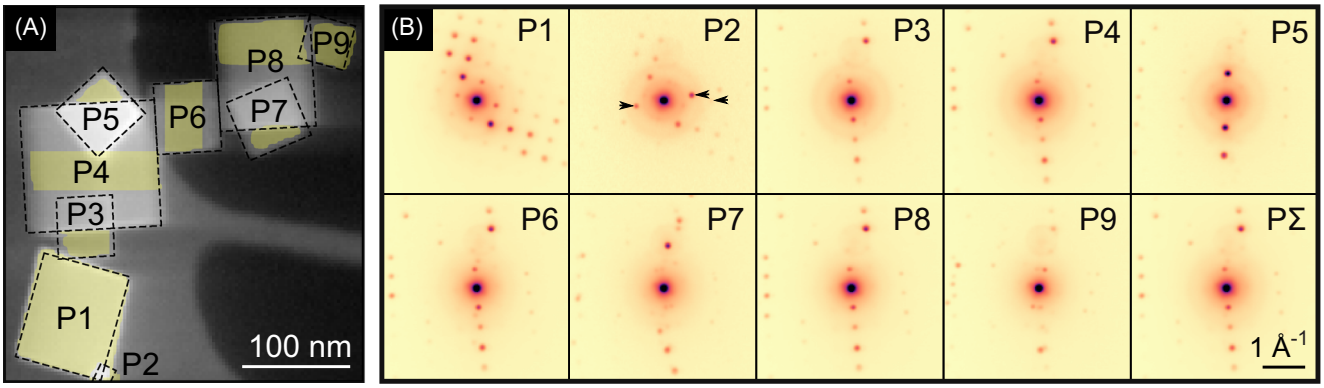

Fig. 3. (A) Annular virtual dark-field (VDF) image showing nine magnesium oxide (MgO) particles (grey), labelled P1–P9, lying on top of a holey amorphous carbon film (dark grey) or over vacuum (black). The outlines of the MgO particles are indicated by dashed rectangles. (B) Sum of PED patterns within the yellow areas in (A). The detected diffraction vectors of P2 are marked by black arrows. PΣ is the sum of P3, P4, P6 and P8.

patterns. The NMF decomposition into E components then produced a stack of component patterns, $C_P\,(E|K_X, K_Y)$, and a corresponding stack of loadings, $C_L\,(E|X, Y)$.

Cross-correlation of both the component patterns and loading maps was performed to merge components that originated from the same crystal, since NMF can result in splitting of signal from one crystal into several components. The correlation step is depicted in Figure 2(B). If the normalized cross-correlation of both the component patterns and loadings exceeded a user-specified *pattern correlation threshold* and a user-specified *loading correlation threshold*, respectively, component patterns and loadings were summed. This correlation step resulted in component patterns, $C_{CP}\,(F|K_X, K_Y)$, and loadings, $C_{CL}\,(F|X, Y)$, where $F \leq E$. After correlation, the loadings were segmented by watershed, as portrayed in Figure 2(C), using the same approach as for the VDF images described above. Segments were discarded if their maximum intensities were below a user-defined *minimum intensity threshold* or their total sizes were below a user-specified *minimum size*. Each resulting loading segment was associated with its corresponding component pattern, which resulted in component patterns $C_{SP}\,(G|K_X, K_Y)$, and loading segments, $C_{SL}\,(E|X, Y)$, where $G \geq F$.

Results and discussion

SPED data inspection

An annular VDF image formed using the demonstration SPED dataset D is shown in Figure 3(A), where the outline of each of the nine cubic particles, labelled P1–P9, are indicated. Figure 3(B) shows the sum of PED patterns within a region without overlap for each particle, except for P2 that overlapped significantly with P1. The detected diffraction vectors of P2 are indicated in (B). P3, P4, P6 and P8 had similar orientations, as seen by the morphological similarities in (A) and the similar PED patterns in (B). The sum of the PED patterns of these particles, labelled PΣ, is also shown in (B).

VDF imaging-based segmentation

The results of VDF imaging-based segmentation are shown in Figure 4. Figure 4(A) shows summed VDF image segments (V_{SS}), and (B) shows the corresponding virtual diffraction patterns (P_D). P1 and P4–P9 were segmented and labelled V1 and V4–V9, respectively. P2 was not included in the segmentation results, since only a few diffraction vectors were detected for this particle (Fig. 3B), so that it was excluded by the *vector threshold* criteria. This criterion was incorporated to allow exclusion of segments resulting from noise or particles not being separated correctly. P3 was not segmented and was included in V4 together with P4 (Fig. 4A), since P3 and P4 did not display sufficient differences in their VDF images. These two particles shared the same orientation and had only common diffraction vectors (Fig. 3B), which meant that they appeared exclusively in the same VDF images where they always overlapped. Most often, only one marker was defined for both particles (e.g. Fig. 1B), which lead to both being included in the same segment after watershed segmentation. Thus, regions were only segmented if they displayed a minimum number of detectable diffraction peaks, and if they displayed sufficient distinctness in the VDF images to allow marker detection and to give clear edges in the elevation images for watershed segmentation.

Figure 4(C) shows preprocessed PED patterns from regions without overlap where the diffraction vectors found in the virtual diffraction patterns are marked. Figure 4(D) shows the difference between normalized preprocessed PED patterns and normalized virtual diffraction patterns. Some diffraction vectors were missing in the reconstructed virtual diffraction patterns, and the difference patterns, especially P4–V4, P8–V8 and P9–V9, displayed large residuals where strong peaks were not included fully in the virtual diffraction patterns. Some

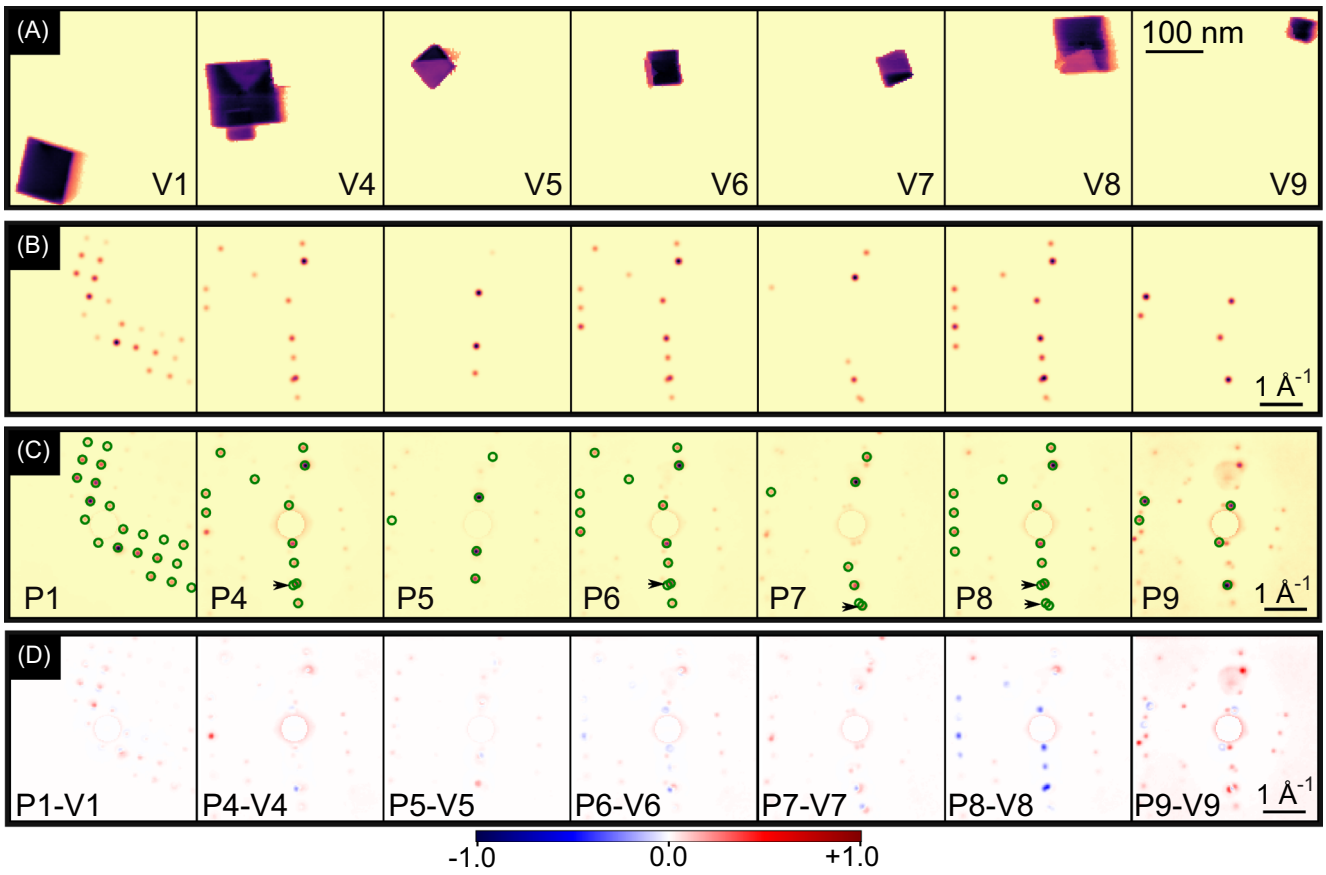

Fig. 4. Virtual dark-field (VDF) imaging-based segmentation results. (A) Summed VDF image segments (V_{SS}), labelled V1 and V4–V9 according to the particle numbering in Figure 3, and (B) corresponding virtual diffraction patterns (P_D). (C) Sum of preprocessed precession electron diffraction (PED) patterns within the regions indicated in Figure 3(A). The diffraction vectors found in the virtual diffraction patterns (B) are encircled in green, and the black arrows indicate positions where the virtual apertures of two vectors overlapped. (D) Difference between the preprocessed sum PED patterns (C) and the corresponding virtual diffraction patterns (B), after normalization.

vectors were left out because of incorrect segmentation in the corresponding VDF images. Incorrect segmentation resulted from inhomogeneous intensity distributions or noise in the VDF images that lead to an inappropriate choice of markers and/or elevation images that did not reflect the particle shapes. In a worst-case scenario, an incorrectly shaped segment could give a sufficiently high correlation score with a correctly shaped segment, giving a false positive result. Furthermore, two diffraction peaks were included in the virtual diffraction patterns at some positions where only one peak was observed in the reference PED pattern, as marked in Figure 4(C). For these peaks, the virtual apertures overlapped, which meant that intensity from one peak contributed to two VDF images. Another consequence of using a virtual aperture was that the virtual diffraction patterns did not contain any information on the intensity distribution associated with the diffraction vectors. This resulted in prominent residuals in the difference patterns near diffraction vectors, e.g. asymmetric annuli in P9–V9.

NMF-based segmentation

The results obtained by NMF are shown in Figure 5. For NMF, the number of components, E, was a required parameter. By inspection, eight source signals could be identified in the dataset, i.e. six distinct MgO crystal orientations, amorphous carbon and vacuum (Fig. 3). However, the appropriate number of components for the decomposition could be higher, due to thickness or background intensity variations, strain, bending or crystal defects. In general, the scree plot produced by SVD can be used as a guide to estimate the number of components (Martineau *et al.*, 2019). Assuming that components describing signals account for the largest fractions of variance in the data, the number of components at which the amount of variance is relatively low and starts to decay slowly is typically considered an appropriate choice, as the components after that point should describe noise. In that case, the scree plot would show an 'elbow' or 'knee' shape. The scree plot associated with SVD of the SPED data is shown in Figure 5(A), and a notable gap in fraction of variance can be discerned

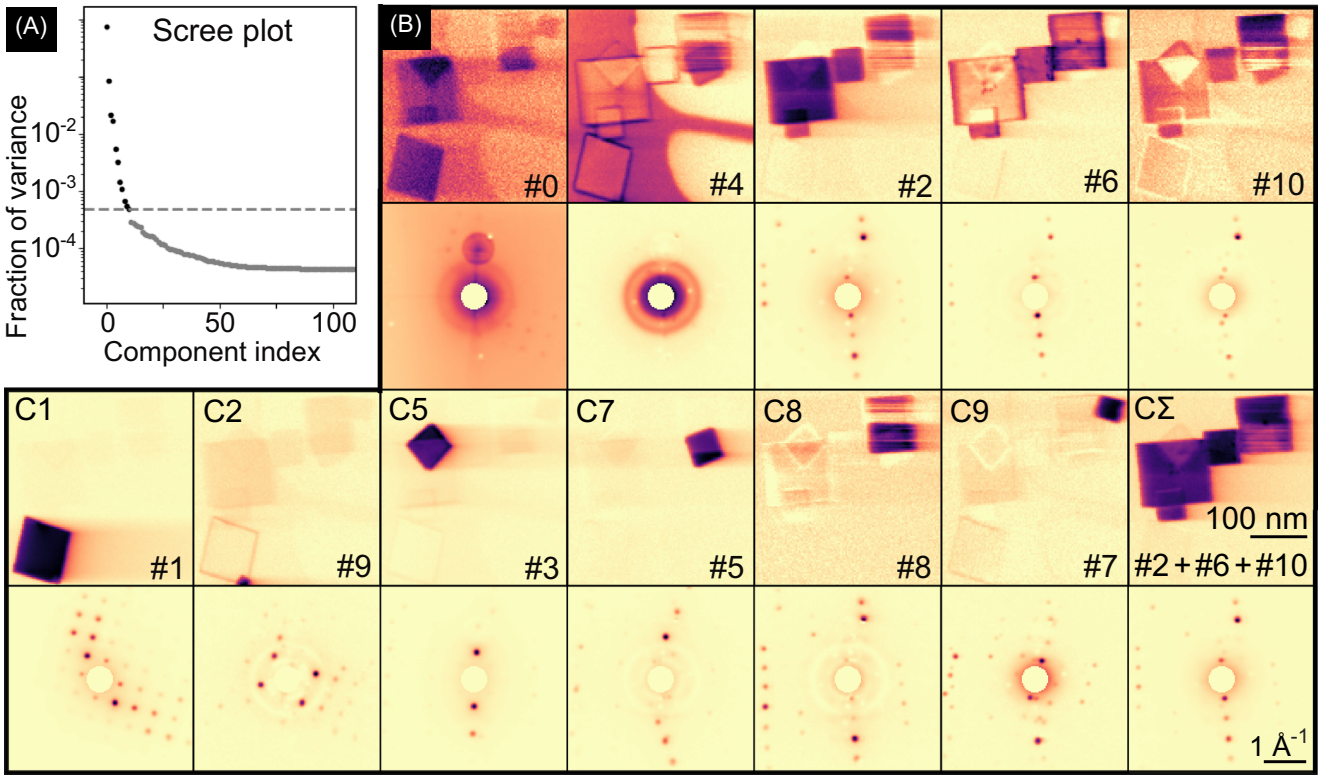

Fig. 5. Non-negative matrix factorization (NMF) results. (A) Singular value decomposition (SVD) scree plot showing the fraction of total variance that each component accounted for. The dashed horizontal line indicates that a number of 11 components was used for NMF. (B) Component patterns (top) and corresponding loading maps (bottom) obtained by NMF, labelled #0-#10. The component patterns and loadings after correlation are labelled C1–C9, according to the particle labelling in Figure 3, and CΣ is the sum of components #2, #6 and #10.

after 11 components, which was the number of components chosen for NMF.

The component patterns (C_P) and loadings (C_L) obtained by NMF, labelled #0-#10, are shown in Figure 5(B). Components #1-#3 and #5-#10 were all related to MgO particles, whereas #0 was related to background and glare from the recording system, and #4 was related to the carbon film. Therefore, components #0 and #4 were discarded prior to the correlation step, which was performed to merge components related to the same crystals. The component patterns and loadings resulting from correlation (C_{CP} and C_{CL}) were labelled C1–C2, C5–C9 and CΣ according to the particle labelling. CΣ resulted from addition of components #2, #6 and #10, which were all related to particles that shared the same orientation; P3, P4, P6 and P8. None of the other components were merged during the correlation step, since they represented individual particles of different orientations and therefore gave low correlation values to the other components. P8 was partly accounted for both by components C8 and CΣ, which indicated that P8 comprised PED patterns that could be grouped mainly into two different diffraction conditions.

After correlation, the loading maps were segmented by watershed, and the resulting loading segments (C_{SL}), labelled CS1–CS7, CS8i–CS8iii and CS9, are shown in Figure 6(A). CS1, CS5–CS7, CS8iii and CS9 corresponded to the individual particles P1, P5–P7, P8 and P9, respectively. CS2 corresponded to P2, but also included weaker intensities from surrounding regions that were not sufficiently removed by automatic thresholding, but that could have been removed by additional manual thresholding. CS4 contained signals both related to P3 and P4 for the same reason as explained previously for V4. P8 was split into three segments, CS8i–CS8iii, where the first two resulted from C8 and the last from CΣ, since this particle gave rise to more than one unique PED pattern, as mentioned earlier.

Figure 6(B) shows the difference between the PED patterns (Fig. 3B) and the corresponding component patterns (Fig. 5B), after normalization. Pseudo-subtractive intensities, i.e. regions where intensity was apparently missing, could be observed in some component patterns, e.g. #7-#9, similar to observations in Martineau *et al.* (2019), which gave positive residuals in the difference patterns, e.g. P2–C2, P8–C8 and P9–C9. Also, the difference patterns showed positive background intensities, since the background was accounted for largely by component #0. Moreover, there were notable residuals related to diffraction vector intensities, even for cases

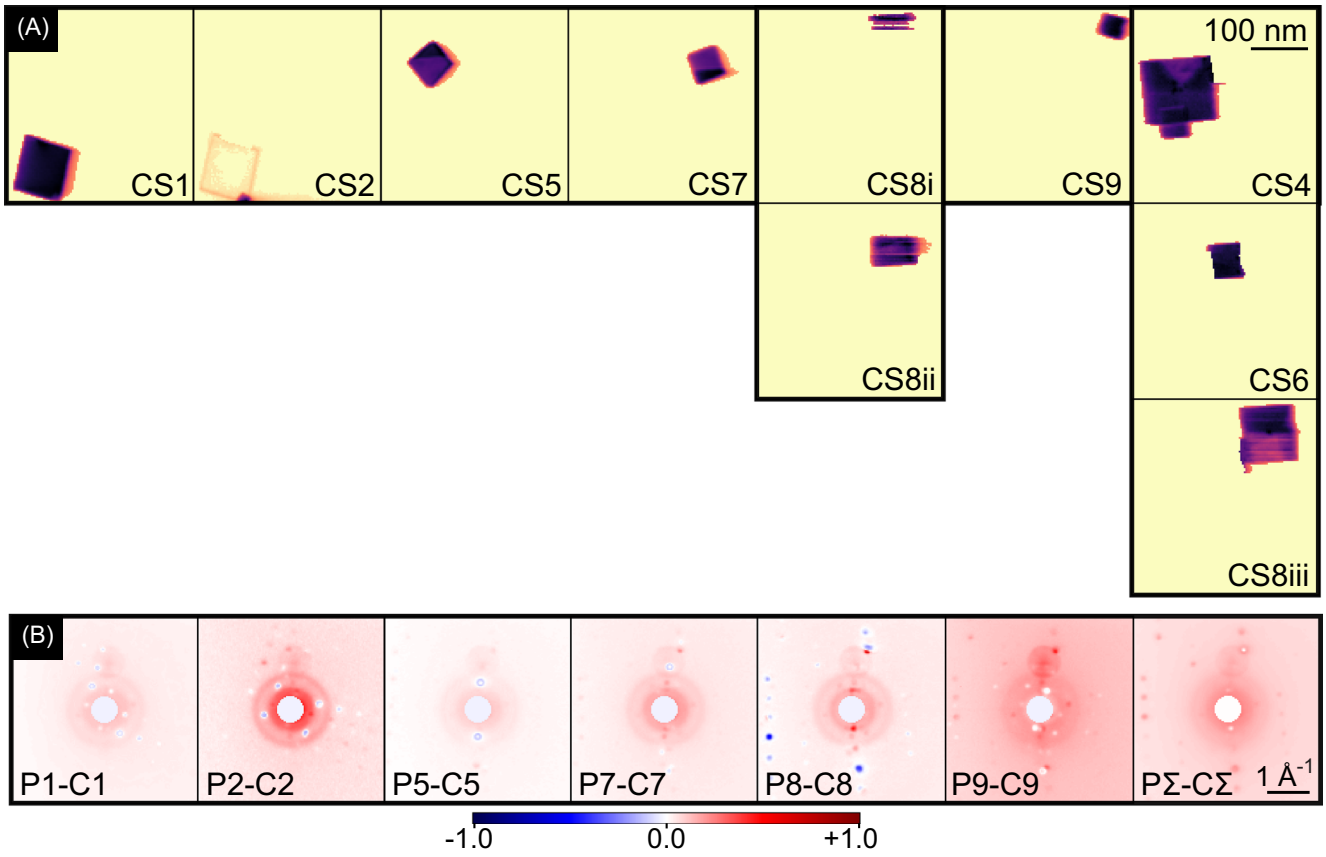

Fig. 6. Non-negative matrix factorization (NMF)-based segmentation results. (A) Loading map segments, labelled CS1–CS7, CS8i–CS8iii and CS9 according to the particle labelling (Fig. 3), resulting from watershed segmentation of the correlated component loading maps (Fig. 5B). (B) Difference between precession electron diffraction (PED) patterns (Fig. 3B) and the corresponding component patterns (Fig. 5B), after normalization.

where the PED pattern and the component pattern corresponded to highly similar areas in real space, e.g. negative values $\lesssim 0.06$ could be seen in P1–C1.

Comparison of the two nanocrystal segmentation methods

Comparing the results from the VDF imaging- and the NMF-based segmentation methods (Figs. 4–6), it is apparent that both approaches resulted in segmentation of particles P1, P5–P7 and P9. However, P2 was segmented in the NMF-based method and discarded in the VDF imaging-based method (Figs. 4A and 6A). This was because the VDF imaging-based method required that each segment displayed a sufficient number of detectable diffraction peaks, whereas NMF was less restrictive in that all distinct intensities accounting for significant variation in the data could give rise to individual components. That could be advantageous in nanocrystal segmentation as all crystals should be accounted for, given a large enough number of components. On the other hand, it could give complications in physical interpretations, since it is not necessarily diffraction from crystals of distinct orientations that give rise to individual components. Intensities related to individual crystals could be split into several components, which was countered partly in this work by inclusion of a correlation step that enabled the summation of similar components. The correlation step lead to summation of components #2, #6 and #10 and subsequent segmentation of P4 and P6. Contrarily, C8, that was related to parts of P8, did not correlate sufficiently with other components, so that contribution from P8 was split into several segments, C8i–C8iii (Fig. 6A). Consequently, both segmentation approaches should be used with caution so as to avoid disregarding or oversegmenting crystals.

A major difference between the virtual diffraction patterns and the component patterns (Figs. 4B and 5B) was that the component patterns included all major diffraction vectors, whereas the virtual diffraction patterns were missing some. For VDF imaging-based segmentation, incorrect segmentation happened for some vectors, as mentioned earlier. Moreover, peak finding was done for each preprocessed PED pattern individually, and so relatively weak peaks would either not have been detected or could have resulted in noisy VDF images, which could have given incorrect segmentation. NMF was more sensitive in that data redundancy was exploited to pick

out even weak, recurring intensities, given a large enough number of components. Furthermore, the virtual diffraction patterns contained no information about the intensity distribution associated with individual diffraction vectors, as opposed to the component patterns. Thus, the need for and the way of creating virtual diffraction patterns should be critically evaluated. Nonetheless, the difference patterns (Figs. 4D and 6B) showed notable residuals near diffraction vector positions for both methods, which indicated that neither the intensities in the component patterns nor the intensities in the virtual diffraction patterns could necessarily be used quantitatively.

The same watershed segmentation procedure was used for both VDF imaging-based and NMF-based segmentation, and it did not enable distinction of P3 from P4, which lead to P3 being included in the segment of P4 for both methods. One way to resolve such issues could be to include morphological prior knowledge as demonstrated in Hamarneh & Li (2009), here the fact that the crystals are cubes in projection. An alternative may be to apply contour fitting as a part of the segmentation step, similar to the approach demonstrated in Jung & Kim (2010). Such approaches could allow attribution of overlap areas to more than one segment and possibly give segments better reflecting the crystal morphologies.

Conclusions

Two methods for nanocrystal segmentation, based on VDF imaging and NMF, respectively, were applied to SPED data obtained from a model system of partly overlapping MgO nanoparticles. This model system contained crystals that excited the same diffraction conditions and emphasized situations where neither of the methods distinguished all crystals. To overcome this issue, a watershed segmentation routine was included in both methods, which allowed segmentation of crystals that had highly similar diffraction patterns. However, the segmentation was incomplete for a particularly challenging case where crystals that shared the same orientation also overlapped significantly in real space.

The VDF imaging-based segmentation required that each crystal to be segmented exhibited several detectable diffraction peaks, and thus neglected weak peaks and crystals yielding a relatively small number of peaks. Incorrect segmentation happened for some VDF images, so that some diffraction vectors were lacking in the virtual diffraction patterns. Contrary to the virtual diffraction patterns, the component patterns included information on the intensity distribution associated with individual diffraction vectors. Also, the NMF-based segmentation approach required minimal preprocessing and was more sensitive in the sense that no major intensity contribution was neglected and in that subtle intensity variations could be identified. When comparing the original PED patterns with the corresponding component patterns and with the virtual diffraction patterns, notable intensity differences near diffraction peaks were seen for both of the explored methods, which indicated that neither could necessarily be used quantitatively.

Given that they are used with care and that artefacts are considered critically, both VDF imaging- and NMF-based segmentation can be valuable tools for nanocrystal segmentation in SPED data subject to limitations. The workflows developed are available open-source and can be used for analysis of SPED data and as a platform for further developments.

Acknowledgements

Adrian Lervik is acknowledged for MgO specimen preparation, and Håkon Ånes is acknowledged for participating in discussions on unsupervised machine learning.

Funding information

Research Council of Norway: 237900 (SFI Manufacturing) and 197405 (NORTEM); Engineering and Physical Sciences Research Council, UK: EP/R008779/1; European Unions Horizon 2020 research and innovation programme (ESTEEM3): 823717.

References

Bergh, T. (2019) Scanning precession electron diffraction data of partly overlapping magnesium oxide nanoparticles. [Data set]. Zenodo. https://doi.org/10.5281/zenodo.3382874

Beucher, S. & Lantuejoul, C. (1979) Use of watersheds in contour detection. *International Workshop on Image Processing*, Rennes, France, pp. 1–12.

Cooper, D., Denneulin, T., Bernier, N., Béché, A. & Rouviére, J.-L. (2016) Strain mapping of semiconductor specimens with nm-scale resolution in a transmission electron microscope. *Micron* **80**, 145–165.

de la Peña, F., Prestat, E., Fauske, V. *et al.* (2019) hyperspy/hyperspy v1.4.2. https://doi.org/10.5281/zenodo.3249885

Eggeman, A., Krakow, R. & Midgley, P. (2015) Scanning precession electron tomography for three-dimensional nanoscale orientation imaging and crystallographic analysis. *Nat. Commun.* **6**, 7267. https://doi.org/10.1038/ncomms8267

Einsle, J., Eggeman, A., Martineau, B. *et al.* (2018) Nanomagnetic properties of the meteorite cloudy zone. *Proc. Natl. Acad. Sci. USA* **115**(49), E11436–E11445.

Gallagher-Jones, M., Ophus, C., Bustillo, K. *et al.* (2019) Nanoscale mosaicity revealed in peptide microcrystals by scanning electron nanodiffraction. *Commun. Biol.* **2**(1), 1–8.

Hamarneh, G. & Li, X. (2009) Watershed segmentation using prior shape and appearance knowledge. *Image Vision Comput.* **27**(1–2), 59–68.

Johnstone, D., Crout, P., Høgås, S., Bergh, T., Laulainen, J. & Smeets, S. (2019) pyxem/pyxem-demos v0.10.0. https://doi.org/10.5281/zenodo.3533670

Johnstone, D., Crout, P., Laulainen, J. *et al.* (2019) pyxem/pyxem v.0.10.0. https://doi.org/10.5281/zenodo.3533653

Jung, C. & Kim, C. (2010) Segmenting clustered nuclei using H-minima transform-based marker extraction and contour parameterization. *IEEE Trans. Biomed. Eng.* **57**(10), 2600–2604.

Keenan, M. & Kotula, P. (2004) Accounting for Poisson noise in the multivariate analysis of ToF-SIMS spectrum images. *Surf. Interf. Anal.* 203–212. https://doi.org/10.1002/sia.1657

Kobler, A. & Kübel, C. (2017) Challenges in quantitative crystallographic characterization of 3D thin films by ACOM-TEM. *Ultramicroscopy* **173**, 84–94.

Lee, D. & Seung, S. (1999) Learning the parts of objects by non-negative matrix factorization. *Nature* **401**(6755), 788–791.

Martineau, B., Johnstone, D., van Helvoort, A., Midgley, P. & Eggeman, A. (2019) Unsupervised machine learning applied to scanning precession electron diffraction data. *Adv. Struct. Chem. Imag.* **5**(1). https://doi.org/10.1186/s40679-019-0063-3

Meng, Y. & Zuo, J. (2016) Three-dimensional nanostructure determination from a large diffraction data set recorded using scanning electron nanodiffraction. *IUCrJ* **3**, 300–308.

Mu, X., Kobler, A., Wang, D., Chakravadhanula, V., Schlabach, S., Szabó, D., Norby, P. & Kübel, C. (2016) Comprehensive analysis of TEM methods for $LiFePO_4$/$FePO_4$ phase mapping: spectroscopic techniques (EFTEM, STEM-EELS) and STEM diffraction techniques (ACOM-TEM). *Ultramicroscopy* **170**, 10–18.

Pedregosa, F., Varoquaux, G., Gramfort, A. *et al.* (2011) Scikit-learn: machine learning in Python. *J. Mach. Learn. Res.* **12**(1), 2825–2830.

Rauch, E., Portillo, J., Nicolopoulos, S., Bultreys, D., Rouvimov, S. & Moeck, P. (2010) Automated nanocrystal orientation and phase mapping in the transmission electron microscope on the basis of precession electron diffraction. *Z. Kristallogr.* **225**(2–3), 103–109.

Rouviere, J., Armand, B., Martin, Y., Denneulin, T. & Cooper, D. (2013) Improved strain precision with high spatial resolution using nanobeam precession electron diffraction. *Appl. Phys. Lett.* **103**(241913). https://doi.org/10.1063/1.4829154

Valery, A., Rauch, E., Clément, L. & Lorut, F. (2017) Retrieving overlapping crystals information from TEM nano-beam electron diffraction patterns. *J. Microsc.* **268**(2), 208–218.

van der Walt, S., Schönberger, J., Nunez-Iglesias, J. *et al.* (2014) scikit-image: image processing in Python. *PeerJ* **2**(e453). https://doi.org/10.7717/peerj.453

Vincent, R. & Midgley, P. (1994) Double conical beam-rocking system for measurement of integrated electron diffraction intensities. *Ultramicroscopy* **53**(3), 271–282.

Zaefferer, S. (2011) A critical review of orientation microscopy in SEM and TEM. *Cryst. Res. Technol.* **46**(6), 607–628.